Laser induced periodic surface structures on conjugated polymers: Poly(3-hexylthiophene)

Álvaro Rodríguez-Rodríguez[*,†], Esther Rebollar[‡], Michelina Soccio[§], Tiberio A. Ezquerra[†], Daniel R. Rueda[†], Jose Vicente Garcia-Ramos[†], Marta Castillejo[‡] and Mari-Cruz Garcia-Gutiérrez*[*,†].*

[†] Instituto de Estructura de la Materia (IEM-CSIC), Serrano 121, 28006 Madrid, Spain.

[‡] Instituto de Química Física Rocasolano (IQFR-CSIC), Serrano 119, 28006 Madrid, Spain.

[§] Dipartimento di Ingegneria Civile, Chimica, Ambientale e dei Materiali, DICAM-Università di Bologna, via Terracini 28, 40131 Bologna, Italy.

ABSTRACT

In this work, we report on the surface patterning of semiconducting Poly(3-hexylthiophene) (P3HT) thin films by means of Laser Induced Periodic Surface Structures (LIPSS). Two different laser wavelengths, 266 nm and 532 nm, and a broad range of fluences and number of pulses have been used in order to optimize the LIPSS morphology. Ripples period and depth can be tuned by laser parameters. In particular, the high optical absorption of P3HT at 532 nm enables the formation of well-ordered nanostructures with periodicities around 460 nm. Near Edge X-ray Absorption Fine Structure (NEXAFS) and Raman spectroscopy reveal a good chemical stability of P3HT thin films during LIPSS formation. Conducting Atomic Force Microscopy (C-AFM)

performed on the LIPSS reveals a higher electrical conduction in the trenches than in the ridges regions. Resonance Raman spectroscopy and Grazing Incidence Wide Angle X-ray Scattering (GIWAXS) indicate a loss of crystallinity of P3HT thin films during LIPSS formation suggesting melting of the outer polymer surface. This effect produces ridges with lower molecular order than the original thin film. As a consequence of this transformation, the electrical conduction in the ridges becomes lower than that in the trenches.

1. INTRODUCTION

The semiconducting semicrystalline polymer Poly(3-hexylthiophene) (P3HT) has been widely studied as the active layer in organic field-effect transistors (OFET) [1-3] and organic solar cells.[4-7] In organic photovoltaics (OPVs), the dissociated free charges (electrons and holes) are generated at the interface between the donor (e-donor) and acceptor (e-acceptor) phases, and then transported to their respective electrodes, forming the external circuit. Therefore, increasing the interfacial area between the e-donor and e-acceptor phases and limiting the morphology of the heterojunction to the nanoscale are critical for improving the device performance. Several attempts to produce nanostructures of semiconducting polymers have been carried out in order to improve the device efficiencies of P3HT-based polymer solar cells.[8, 9] Nanostructuring approaches such as those using either anodic aluminum oxide (AAO) membranes [10, 11] or Nanoimprint Lithography (NIL) [12, 13] have been successfully accomplished in P3HT. It is well known that molecular order and crystallinity in semiconducting polymers have a significant impact on their physical properties.[14-16] In general, higher crystallinity levels increase the molecular order and enhance charge mobility along chains leading to an improvement of the electrical transport properties of the material. Therefore the knowledge about changes in the

crystalline structure and molecular chain orientation of the polymer nanostructures is essential in order to correlate the structural parameters with the electrical properties.[17] P3HT consists of a relatively stiff main chain of thiophene rings with one hexyl group as side substituent to render the conjugated polymer more soluble in organic solvents. Typically this polymer develops layered crystalline structures with separated main chain and hexyl groups. The π-π stacking of planar polymer backbones leads to delocalization of electronic states across different chains.[18] Regioregular P3HT (RR-P3HT) forms crystal sheets by π−π-stacking of the thiophene rings which stack in such a way that the alkyl side group can crystallize. In addition, as typical semicrystalline polymers, P3HT forms ~10-nm-wide crystalline regions separated by amorphous interlayers.[19-21] Variations in crystallinity and orientation of P3HT under different conditions like thermal processing [22], doping with additives [22] or by confinement [23, 24] have been detected by X-ray scattering techniques. In particular, confining P3HT within nanostructured grooves by NIL induces a 90º backbone reorientation near the grating sidewalls which frustrates the strong tendency of P3HT molecules to orient edge-on relative to substrate and air interfaces in thin films.[25] A similar trend takes place for P3HT infiltrated into AAO membranes where it was found that the P3HT chains inside the nanorods are aligned in the direction normal to the AAO pore wall. Thus, chains in P3HT nanorods have a partial flat-on orientation with respect to the residual polymer film.[26]

Besides common patterning methods, it is also possible to fabricate Laser Induced Periodic Surface Structures (LIPSS) on polymer surfaces.[27, 28] This laser nanostructuring technique can be envisioned as a potential alternative to lithography processes avoiding the necessity of using clean rooms, high vacuum systems or mask fabrication among others. LIPSS in the form of ripples develop on the material surface as a result of irradiation with a linearly polarized laser

beam in such a way that the interference between the incoming and the surface-scattered waves causes an heterogeneous intensity distribution, which together with a feedback mechanism, results in the enhancement of the modulation intensity.[27] The period of the ripples (L) depends on the laser wavelength (λ), on the effective refractive index (n) of the material and on the angle of incidence (θ) of the laser beam with respect to the normal of the sample plane and can be described by the following relation:

$$L=\lambda /(n\text{-}sin\ \theta) \qquad (1)$$

LIPSS have been observed on polymer surfaces by varying both pulse duration ranging from nano- to femtoseconds and laser wavelengths from the IR to the UV spectral regions.[29-32]

In this work, we propose LIPSS as a novel method of surface patterning on thin films of conjugated polymers. We present a precise morphological description of LIPSS on P3HT by Atomic Force Microscopy (AFM) measurements on samples prepared over a broad range of fluences and number of pulses for two different laser wavelengths of 266 and 532 nm. In addition, *in situ* Grazing Incidence X-ray Scattering (GIXS) experiments at small angle (GISAXS) and wide angle (GIWAXS) have been performed during LIPSS formation in order to investigate the mechanisms involved and the possible changes in sample crystallinity and molecular chain orientation. Supported by Near Edge X-Ray Absorption Fine Structure (NEXAFS) and Raman spectroscopy, we reveal the weak impact of laser irradiation on the chemical integrity of P3HT during LIPSS formation. Structural variation of samples has been correlated to the electrical properties at the nanoscale by means of Conductive AFM (C-AFM) measurements.

2. EXPERIMENTAL SECTION

2.1 Materials

Poly(3-hexylthiophene) was purchased from Ossila (M_w=34100 g/mol, PDI= 1.7; regioregularity= 94.7%). Thin polymer films were prepared by spin-coating on the polished surface of silicon wafers (100) (ACM, France). The wafers were previously cleaned with acetone and isopropanol. A solution of P3HT in chlorobenzene (24 mg/mL) was prepared and stirred at 30^{o}C for 1 hour. A fixed amount of 0.1 mL of polymer solution was dropped by a syringe on a square silicon substrate placed in the center of a rotating metallic horizontal plate. A rotation rate of 2400 rpm was kept during 60 s. For the C-AFM measurements, thin films were prepared on Arsenic *n*-doped Silicon substrates (resistivity ~ 0.001 Ωcm) (Wafer World Inc.) under the same conditions. For NEXAFS measurements, P3HT were spin-coated on silicon substrates, then floated off into a very dilute NaOH/water solution (0.25 wt%) and finally picked up with Transmission Electron Microscopy (TEM) grids. The thickness of the obtained thin films was 140±20 nm with a roughness of a few nanometers, both measured by AFM.

2.2 Laser Irradiation

Laser irradiation was carried out in ambient air conditions at normal incidence with a linearly polarized laser beam of a Q-switched Nd:YAG laser (Lotis TII LS-2131M, pulse duration of 8 ns) at two different wavelengths, i.e. with the second (532 nm) and fourth harmonic (266 nm) at a repetition rate of 10 Hz. These wavelengths were selected for the experiments since P3HT absorbs efficiently with an absorption coefficient of ~2.0 x 10^5 cm^{-1} at 532 nm [33, 34], and in the range ~0.3 – 0.7 x 10^5 cm^{-1} at 266 nm. [33, 35] The irradiation fluences were determined by measuring the laser energy in front of the sample and considering 5 mm as the diameter of the laser spot.

2.3 Scanning Probe Measurements

AFM measurements were carried out under ambient conditions using a commercial scanning probe microscope (MultiMode 8 equipped with a C-AFM module and the Nanoscope V controller, Bruker). The topography AFM images were collected in tapping mode using silicon probes (NSG30 probes by NT-MDT). Heights and periods were measured in 3 different zones of the sample and analyzed by Nanoscope Analysis 1.50 software (Bruker).

Electrical measurements were performed by C-AFM with conductive tips (Pt-Ir covered Si probes with a low spring constant, k = 0.2 Nm^{-1}, SCM-PIC by Bruker) in contact mode by measuring simultaneously both topography and electrical images. For out-of-plane current measurements, the sample was attached with conductive epoxy (CW2400, Chemtronics.) onto a metal support. In these measurements, the conducting probe makes contact with the sample, acting like a nanoelectrode, and maps a current image at a fixed bias. The bias was applied to the conducting substrate, and the current was measured by a preamplifier.

2.4 Raman Spectroscopy

Raman spectroscopy was accomplished by using a Renishaw Raman InVia Reflex Spectrophotometer, equipped with a Leica Microscope, and an electrically refrigerated CCD camera, with excitation lines at 442 nm (HeCd laser), 532 nm (Nd:YAG laser) and 785 nm (diode laser). The spectra were acquired with a spectral resolution of 2 cm^{-1} using a 50× of magnification objective to a spot with a diameter < 1 μm on the samples. Laser power conditions were those that ensure the integrity of the polymer.

2.5 Grazing Incidence X-ray Scattering

In situ GIXS-LIPSS experiments were performed at the DUBBLE beamline [36] of the European Synchrotron Radiation Facility (ESRF, Grenoble, France) as previously described.[37] For LIPSS formation on the polymer spin-coated films we used the second harmonic (λ= 532 nm) of the Q-switched Nd:YAG laser mentioned above at a repetition rate of 10 Hz and at a fluence of 26 mJ/cm^2. For GIXS measurements, an X-ray wavelength of λ= 0.103 nm and a beam size (HxV) of (0.8x0.1) mm^2 were employed. The GIWAXS patterns were recorded, while simultaneous laser irradiation on the sample was taking place, by a Frelon detector (1024 x 1024 pixels, 93.6 x 93.6 μm^2 pixel size) which was located at 105.5 mm from the sample position. The GISAXS patterns were recorded by a Pilatus 1M detector (981 × 1043 pixels, 172.0 x 172.0 μm^2 pixel size) which was located at 6.825 m from the sample position. The sample was mounted horizontally and parallel to the X-ray beam in grazing incidence geometry at a height which intercepted half of the beam intensity.[28, 38] Then, the sample was tilted in order to define an incidence angle between the sample surface and the X-ray beam of α_i=0.4 º, which was above the critical angle of P3HT for X-rays. With this configuration it was possible to detect the structure of the full film thickness. The precise alignment of the laser beam was required in order to reach the sample surface perpendicularly, being the laser polarization vector parallel to the X-ray beam. In order to follow *in situ* the LIPSS formation, both laser irradiation and GIXS acquisition were simultaneously activated. Acquisition time was 5 s. Patterns were analyzed by the Fit2D software.[39]

2.6 Near Edge X-ray Absorption Fine Structure

NEXAFS spectroscopy based on Scanning Transmission X-ray Microscopy (STXM), was performed at the PolLux beamline at the Swiss Light Source, Paul Scherrer Institute, Villigen, Switzerland as described elsewhere. [40] Analysis of spectra was performed by the aXis2000

software package.[41] Thin films on TEM grids were mounted in the sample chamber which was evacuated to low vacuum. The transmitted X-ray intensity through the film was recorded using a scintillator and a photo-multiplier tube and measured as a function of energy (270.0 to 350.0 eV with a resolution of 0.1 eV). Transmitted X-ray intensity was converted to an X-ray optical density, defined as $OD = ln\ (I_0/I)$ by recording the X-ray intensity (I_0) through an empty TEM grid.

3. RESULTS AND DISCUSSION

3.1 LIPSS fabrication on P3HT thin films

We have studied the influence of the number of pulses and laser fluence on the LIPSS morphology at laser wavelengths of 532 nm and 266 nm by means of AFM.

3.1.1 Dependence on the number of pulses and the fluence at 532 nm

Typical nanostructures obtained at λ= 532 nm with different number of pulses and fluence are shown in Figures 1 and 2 respectively. In both cases well-ordered ripples are created. Ripple periods and depths for samples irradiated at different fluences and number of pulses are represented in Figure 3 for the wavelength of 532 nm. As we have previously reported for mainly amorphous aromatic polyesters at 266 nm, at constant fluence, [27, 28] the LIPSS period increases with the number of pulses. In this case, the period increases up to ~4500 pulses and reaches a plateau (Figure 3a) with a value slightly smaller than the laser wavelength, and decreases after about 10000 pulses. The depth of the ripples follows a similar tendency as a function of the number of pulses, increasing up to 90 nm for ~4500 pulses (Figure 3a). The dependence of the period of LIPSS with the fluence at 3600 pulses is presented in Figure 3b.

This number of pulses was selected to ensure LIPSS with good quality are obtained for several laser fluences. The figure shows that the period slightly increases up to a fluence of about 26 mJ/cm^2 and remains practically constant afterward. Above 50 mJ/cm^2 the ripples start to deteriorate. Regarding the depth of the ripples, and similarly to what is observed in the dependence with the number of pulses, it increases up to 100 nm for 40 mJ/cm^2 reaching a plateau above this fluence value (Figure 3b).

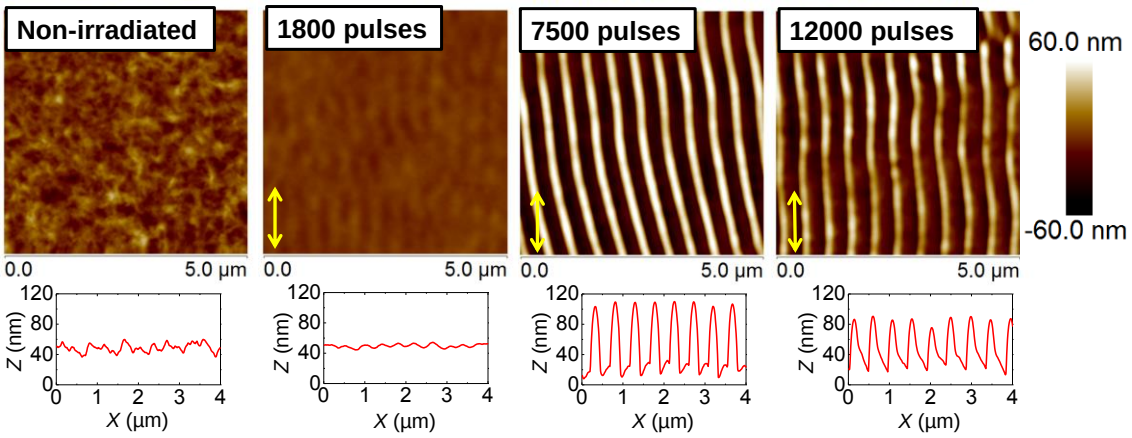

Figure 1. AFM height images of LIPSS on P3HT thin films at a fixed fluence of 26 mJ/cm^2 by varying the number of pulses. Laser irradiation wavelength λ= 532 nm. Height profiles over lengths of 4 µm are shown at the bottom of the images. The double arrows indicate the polarization vector of the laser beam.

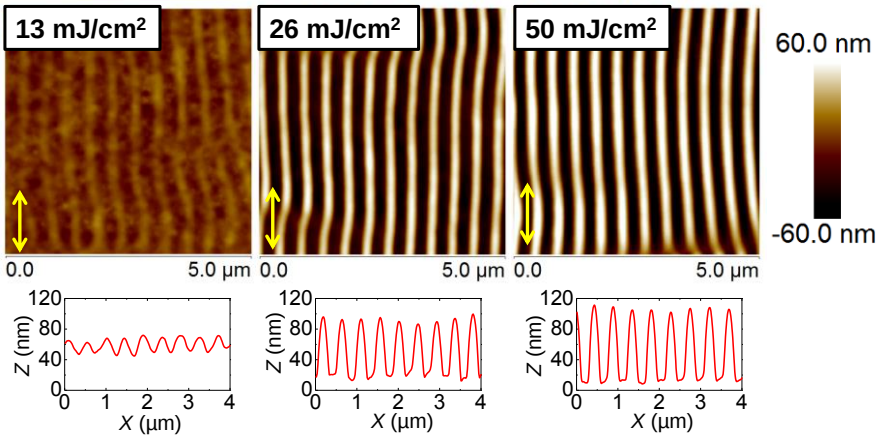

Figure 2. AFM height images of LIPSS on P3HT thin films created with 3600 pulses varying the fluence. Laser irradiation wavelength λ= 532 nm. Height profiles over lengths of 4 µm are shown at the bottom of the images. The double arrows indicate the polarization vector of the laser beam.

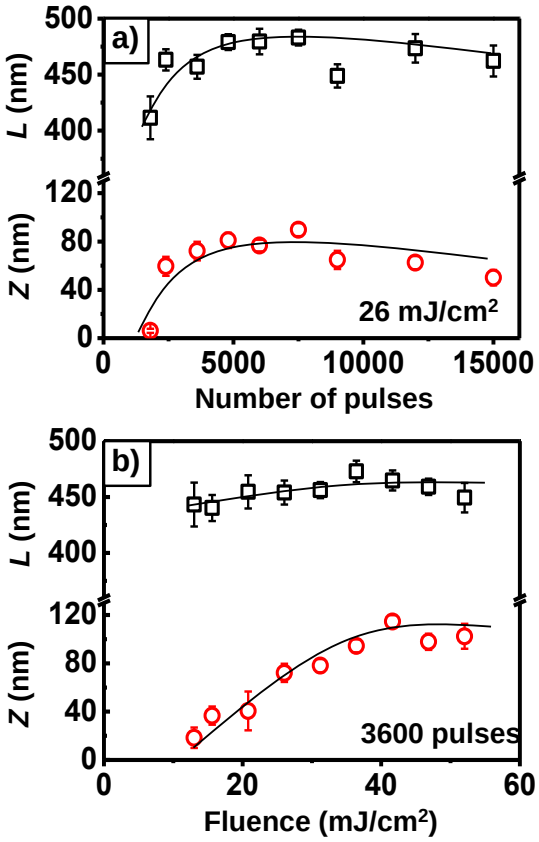

Figure 3. Variation of periods (L) and depths (Z) of LIPSS as a function of (a) number of pulses and (b) fluence for the laser irradiation wavelength λ= 532 nm. Lines are shown as visual guides.

In situ GISAXS experiments have been performed during LIPSS formation. Figure 4 shows characteristic GISAXS patterns of P3HT irradiated at 26 mJ/cm^2 for different number of pulses. Scattering maxima out of the meridian (i.e., for $q_y \neq 0$) are clearly visible in the range of pulses in which LIPSS formation is observed. In a first approach, the period L of the nanostructures can be determined through the expression $L = 2\pi/q_y^{MAX}$, where q_y^{MAX} is the reciprocal scattering vector corresponding to the first intensity maximum[28] next to $q_y = 0$. The long period derived from GISAXS patterns of the irradiated polymer at different number of pulses shows an almost

constant value of about 375±10 nm. As we have reported in previous works[27, 28] the values obtained by GISAXS are systematically lower than the ones obtained by AFM.

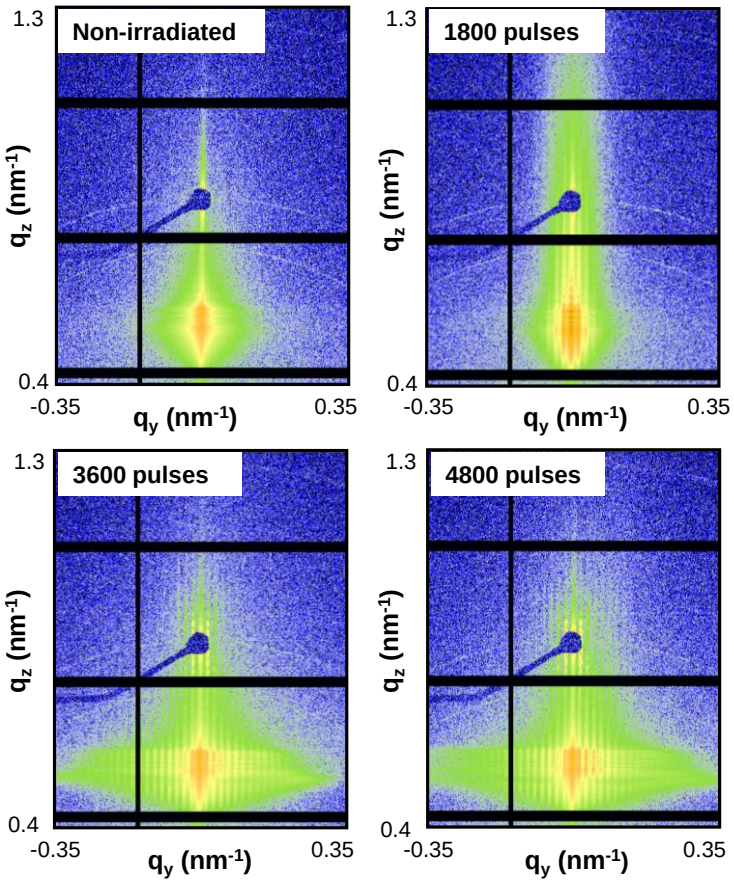

Figure 4. Experimental GISAXS patterns of P3HT irradiated at 26 mJ/cm^2 for different amount of pulses as labeled on the upper left corner.

3.1.2 Dependence on the number of pulses and the fluence at 266 nm.

Figure 5a shows the dependence of period and depth of ripples generated at 266 nm as a function of number of pulses at a constant fluence of 13.4 mJ/cm^2. The period remains constant for about 2500 pulses, and subsequently increases reaching a plateau with a value close to the laser wavelength upon irradiation with 5500 pulses. The variation of LIPSS depth as a function of

number of pulses (Figure 5a) follows a similar behavior, increasing up to 5000 pulses and reaching a plateau of about 70 nm. The dependence of the LIPSS period with the fluence at 3600 pulses is presented in Figure 5b. The period increases up to a value of about 14 mJ/cm^2 and remains practically constant at a value close to the irradiation wavelength. Regarding the depth of ripples, and similarly to what is observed in the dependence with number of pulses, it increases up to 85 nm for 14 mJ/cm^2 reaching a plateau at higher fluence values (Figure 5b). Above 14.7 mJ/cm^2 the ripples start to deteriorate.

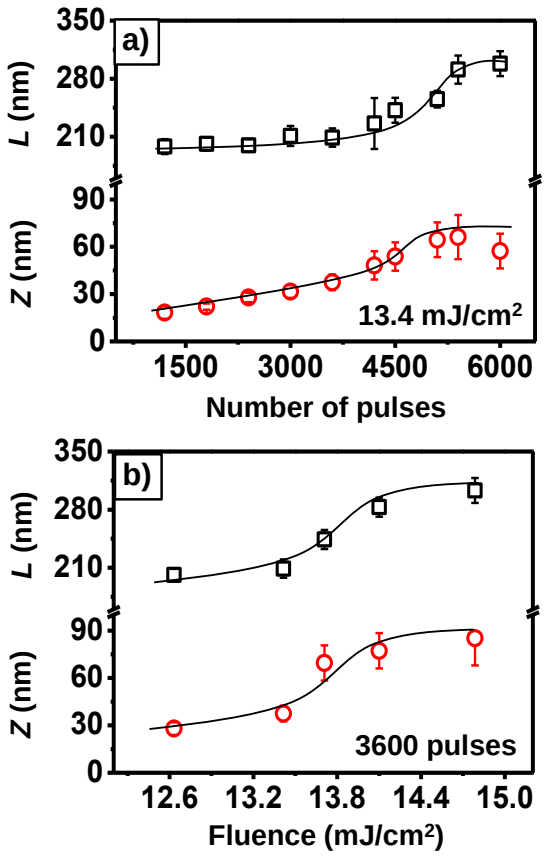

Figure 5. Variation of periods (*L*) and depths (*Z*) of LIPSS as a function of (a) number of pulses and (b) fluence for the laser irradiation wavelength λ= 266 nm. Lines are shown as visual guides.

We have reported previously that in order to obtain LIPSS in amorphous polymers, a minimum fluence value is necessary to ensure that the surface temperature overcomes the glass transition temperature (T_g) [27] and therefore allowing polymer segmental and chain dynamics. In the case of semicrystalline polymers, such as regioregular P3HT, the thermal properties are governed not only by the glass transition temperature but also by the melting temperature (T_m) [27]. It means that in the range of fluences for which LIPSS are obtained the temperature reached at sample surface is higher than T_m and as a result superficial crystallites are melted providing enough polymer dynamics.

Topography AFM images of the optimal P3HT LIPSS obtained for the two laser wavelengths used are shown in Figure 6. The values of the periods are close to the wavelength of the laser in agreement with equation 1. LIPSS fabricated at 266 nm present structures with lower degree of order than those created with the irradiation wavelength of 532 nm. Differences in the quality of the structures (regular lengths and size of the ripples) are related to the absorption coefficient of the material at each wavelength. The higher absorption coefficient of P3HT at 532 nm in relation to 266 nm (α_{266}= 0.3-0.7·10^5 cm^{-1} vs. α_{532}=2·10^5 cm-^{1}), [33, 34] leads to the formation of better ordered ripples than those observed for irradiation at λ=266 nm. However, formation of LIPSS has been reported for polymers with absorption coefficient as low as 3000 cm^{-1}. This is the case of polystyrene at 248 nm[43] for which LIPSS have been reported upon irradiation at fluences in the range 7-9 mJ/cm^2 after a few thousand of pulses[42]. Therefore, there should be another reason accounting for LIPSS of less quality than those obtained at the visible wavelength. One possibility is the fact that hexylthiophenes with low molecular weight (oligomers) absorb efficiently in the region of 266 nm while a higher degree of conjugation induces a shift in the absorption band towards larger wavelengths (around 500 nm). Therefore, in the UV-visible

spectrum of P3HT the absorption at 266 nm is attributed to oligomers [44-46] and the LIPSS mechanism is less efficient. Since LIPSS at 532 nm presents more regular ripples, we have performed a complete characterization in the structures created at this wavelength.

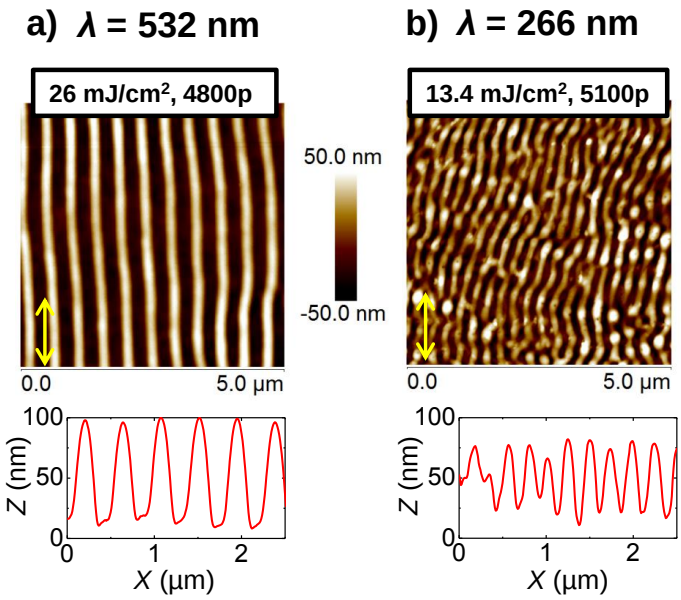

Figure 6. AFM height images of optimal LIPSS obtained on P3HT thin films: a) at 532 nm, fluence of 26 mJ/cm^2 and 4800 pulses and b) at 266 nm, fluence of 13.4 mJ/cm^2 and 5100 pulses. Height profiles over lengths of 2.5 µm are shown at the bottom of each image. The polarization vector of the laser beam is indicated by double arrows.

3.2 Electrical characterization by Conductive-AFM

C-AFM was used to characterize the electrical properties at the nanoscale of LIPSS produced by irradiating a P3HT thin film at 532 nm. Figure 7 shows the C-AFM current images (electric current map), acquired in contact mode, of a P3HT thin film sample before irradiation (Figure 7a) and after irradiation with a fluence of 26 mJ/cm^2 and 4800 pulses (Figure 7b) by applying a constant voltage of -5 V on the conducting substrate. The current image of the sample before

irradiation shows that the thin film is conductive in the whole area, while the image displaying the current map of the irradiated thin polymer film shows stripes with a similar conductivity to the initial thin film separated by nonconductive ones. It is worth to notice that C-AFM measurements performed in P3HT films with different thicknesses, ranging from 50 nm to 350 nm, revealed that all of them were conductive. Thus it can be established that the observed effect in Figure 7b is not caused by the thickness difference between trenches and ridges. In order to correlate conductive regions with either trenches (bottom) or ridges (top) observed in the height image, we have overlapped topography and current images in Figure 7c.

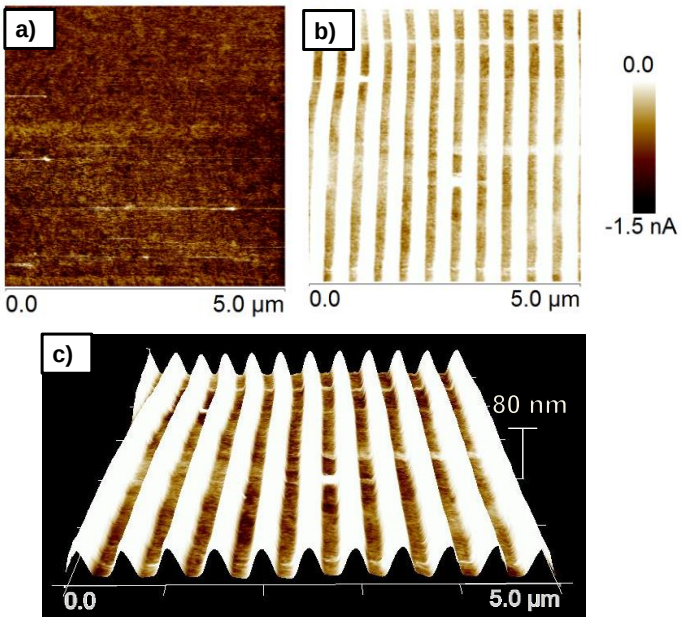

Figure 7. C-AFM current images of a P3HT thin film measured at a constant bias of -5 V. a) Non-irradiated film, b) film with LIPSS fabricated at 532 nm, 26 mJ/cm^2 and 4800 pulses. c) Overlap of height and current images of P3HT with LIPSS. Height scale is 80 nm.

We observe that conductive regions correspond to trenches and non-conductive regions to ridges. This fact might be attributed in principle either to selective chemical damage due to laser

irradiation or to reorganization of the polymer chains and therefore to possible structural changes like partial loss of crystallinity in the ridges. These two aspects will be addressed in the following paragraphs.

3.3 Chemical stability and structural modification in nanostructured P3HT thin films.

3.3.1 Near Edge X-ray Absorption Fine Structure

NEXAFS experiments were performed in order to gain further information about the chemical stability of the P3HT thin films after laser irradiation at 532 nm. A NEXAFS spectrum in the K-edge reveals the excitation of 1s electrons to unfilled molecular orbitals. The NEXAFS spectra in the carbon K-edge of pristine thin films and of those with LIPSS are presented in Figure 8. The shape of the spectra is the expected one for P3HT.[47, 48] The sharp peak at 285 eV (C1s → π* transitions) is characteristic of the strong electronic delocalization along the conjugated backbone of thiophene rings and therefore very sensitive to differences in the polymer π-backbone. Other characteristic peaks are assigned to C1s → σ*(C–H) transitions at approximately 287-288 eV, corresponding to the hexyl group, and to a broad set of C1s → σ* C–C transitions near 293 eV. [48] Overall, NEXAFS results suggest the absence of significant changes in the chemical structure of P3HT after LIPSS formation.

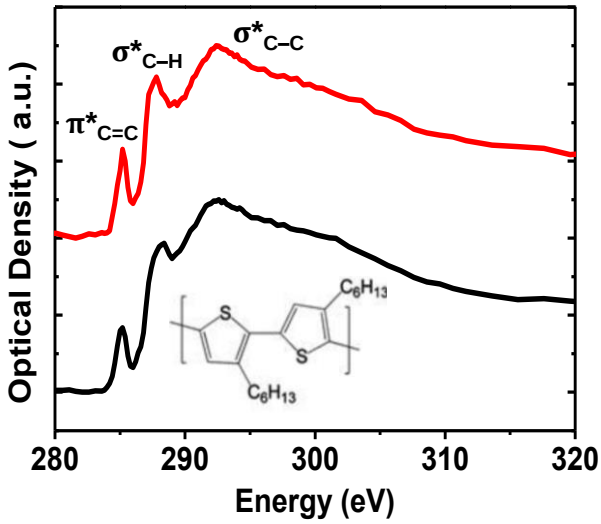

Figure 8. NEXAFS spectra in the carbon K-edge of P3HT (chemical structure shown) thin film (red line) and of P3HT film with LIPSS fabricated at 532 nm, 26 mJ/cm^2 and 4800 pulses (black line). The spectra have been vertically shifted for clarity.

3.3.2 Raman spectroscopy

In order to elucidate the reason of the different electrical properties of ridges and trenches of P3HT films endowed with LIPSS (at 532 nm), we have performed micro-Raman measurements at different excitation conditions (λ_{exc} =785 nm, 532 nm and 442 nm). Figure 9 shows the Raman spectra of P3HT thin films (red) and P3HT with LIPSS fabricated at 532 nm, 26 mJ/cm^2 and 4800 pulses (black) at the different excitation wavelengths employed.

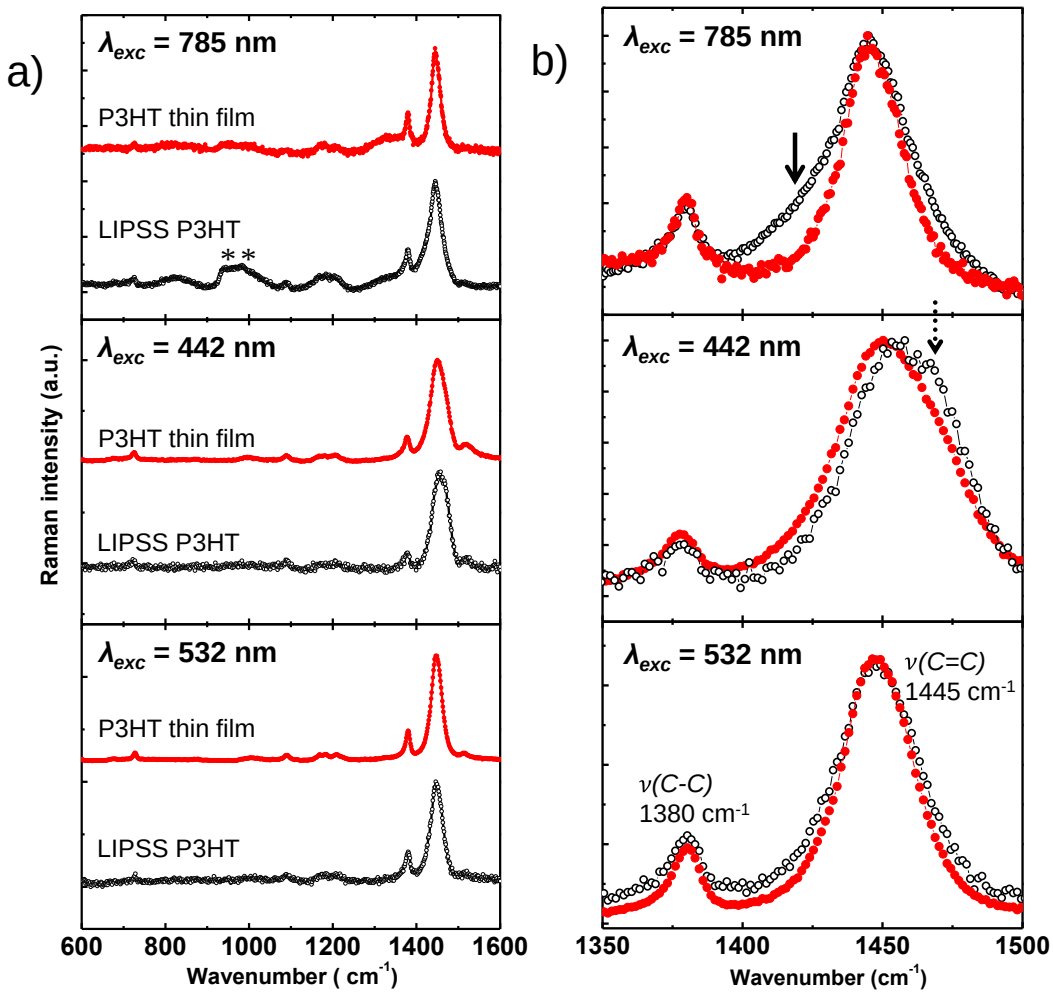

Figure 9. (a) Raman spectra of non-irradiated P3HT thin films (red) and films with LIPSS fabricated at 532 nm, 26 mJ/cm^2 and 4800 pulses (black) under different excitation wavelengths. (b) Comparison of the ν(C=C) band region before (red) and after laser irradiation (black). The continuous and dotted arrows indicate the νC=C) vibration of the quinoid form and amorphous phase respectively. Star marks (**) in Figure 8a (top) correspond to silicon bands.

The spectra present characteristic bands at 1445 cm^{-1} and 1380 cm^{-1} which can be assigned to the symmetric stretching mode of the C=C and C-C intra-rings bonds respectively.[49] In particular we

focus on the 1350−1500 cm^{-1} spectral range (enlarged in Figure 9b), known to be the active Raman region sensitive to the π-electron delocalization (i.e., related to the conjugation length and optical absorption) of the P3HT chains.[49, 50] It is well known that regioregular P3HT (RR-P3HT) thin films present optical absorption between 400 and 600 nm. [33, 51] This indicates that at 785 nm excitation occurs under non-resonance conditions while excitation at 532 nm and 442 nm leads to measurements under resonance conditions. The spectra obtained under non-resonance conditions (λ_{exc}=785 nm) exhibit similar positions for the ν(C=C) band (symmetric stretching mode) for both the non-irradiated films and those with LIPSS. There is no evidence of new bands suggesting that the P3HT thin films are relatively stable under the irradiation conditions used for fabricating LIPSS. In addition, the peak intensity ratio between the two bands at 1380 cm^{-1} and 1445 cm^{-1} is similar and therefore no significant evidence of P3HT photodegradation exists.[52] The difference between non-irradiated thin films and irradiated (with LIPSS) is emphasized when focusing on the Raman spectra in the 1350−1500 cm^{-1} spectral range shown in Figure 9b (top). A detailed inspection reveals the appearance of a shoulder at 1420 cm^{-1} (marked by a continuous arrow) on the lower wavenumber region of the ν(C=C) band. This shoulder is assigned to the stretching of the C=C bond of the quinoid form of P3HT due to the oxidation of the aromatic backbone.[53-55] However, under resonance conditions the results are quite different. At this point it is worth mentioning that the optical absorption of RR-P3HT in solution presents an absorption maximum near 400 nm while RR-P3HT thin films present a red-shift of absorption maximum up to 600 nm. This fact is due to the difference in conjugation length between RR-P3HT in solution (disordered) and RR-P3HT thin films (partially ordered).[47] In principle, polymer segments in ordered regions should exhibit higher conjugation length than those located in the amorphous regions. Therefore in RR-P3HT thin films, the absorption near 400 nm is

associated to the disordered chains whereas absorption near 600 nm is associated to ordered chains.[50, 56] Thus, in the Raman spectra under resonance conditions at λ_{exc}= 442 nm, corresponding to a region of high absorption for disordered P3HT chains, the ν(C=C) band shifts towards higher wavenumbers where it also presents a shoulder, marked by a dotted arrow in Figure 9b (center). It has been reported [49, 57] that under resonance conditions, the intensity of Raman bands from disordered regions is enhanced. Moreover, the Raman spectra collected at an excitation wavelength of 532 nm, for both the P3HT thin film and the P3HT with LIPSS, does not present noticeable variations in the position of the ν(C=C) band, in similarity to what is observed in the spectra collected at 785 nm. This effect can be related to the fact that under these resonance conditions (λ_{exc} =532 nm), P3HT segments located in ordered regions absorb stronger than those in the amorphous phase.[51] Since the Raman spectra obtained by excitation at λ_{exc} =442 nm present variations, it is possible to deconvolute the Raman bands into their two contributions. The more intense contribution appearing at lower wavenumbers (~1445 cm^{-1}) corresponds to the crystalline phase with a higher conjugation length, while the less intense band (~1470 cm^{-1}) corresponds to the ν(C=C) bonds of the amorphous phase with lower conjugation length.[57]

Figure 10 shows the deconvolution of the ν(C=C) band of non-irradiated P3HT thin film and of that with LIPSS by simple Lorentzians, in accordance to previous works.[57, 58] These results indicate a relative increase of the amorphous phase after laser irradiation.

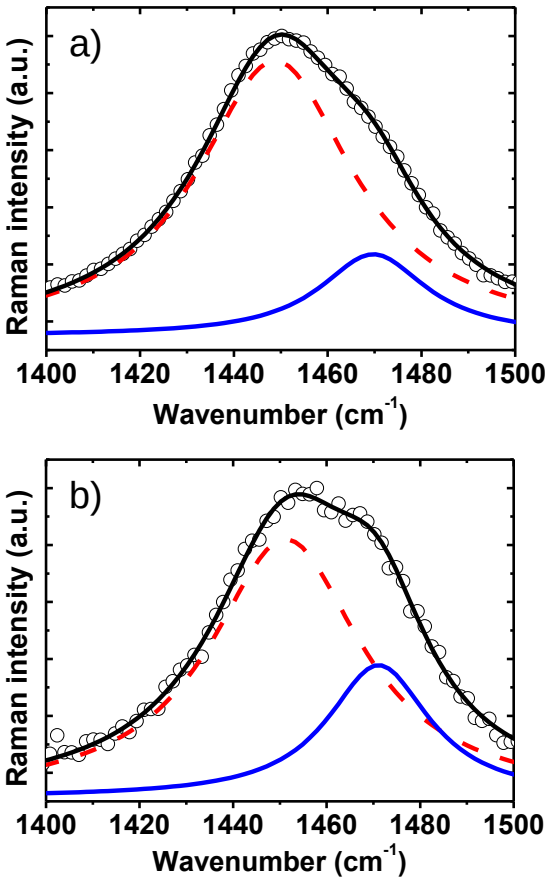

Figure 10. Deconvolution of the ν(C=C) band of the Raman spectra (circles) of a P3HT thin film collected at 442 nm laser excitation (a) before and (b) after LIPSS formation by irradiation at 532 nm, 26 mJ/cm^2 and 4800 pulses. The red dashed line corresponds to the ordered phase and the blue continuous line to the disordered phase. The black continuous line is the fitting of the experimental data.

From Figures 10a and 10b we can estimate the relative fraction of crystalline phase (ϕ) of the P3HT thin film before and after LIPSS formation, by the relation $\phi = A_c/(A_c+A_a)$, where A_c is the area under the red dashed curve (ordered contribution) and A_a is the area under the blue continuous curve (disordered contribution) in Figs.10a y 10b. We obtain values of $\phi_{P3HT} = 0.83$

and $\phi_{P3HT\ LIPSS}=0.71$. As $\phi_{P3HT} > \phi_{P3HT\ LIPSS}$ we can infer that the P3HT loses crystallinity during LIPSS formation. This result can be correlated with the overlapping image of height and current of the sample with LIPSS (Figure 7c). Thus, we propose that the lower conductivity of the ridges can be attributed to an increase of the chain disorder after LIPSS formation. To further support this statement we performed GIWAXS experiments to be discussed in the next paragraph.

3.4. Structural modification of P3HT thin films during LIPSS formation as revealed by GIWAXS

The evolution of the structure of P3HT thin films during LIPSS formation has been investigated by *in situ* GIWAXS experiments using synchrotron radiation. The samples were irradiated at a repetition rate of 10 Hz by using the 2nd harmonic of a Nd:YAG laser (532 nm) with pulses of 8 ns. GIWAXS patterns were acquired during repetitive laser pulse irradiation. The 2D X-ray scattering patterns presented in Figure 10, from the non-irradiated P3HT thin film (Figure 11a) and for the film with LIPSS (Figure 11b) show similar orientation and number of reflections.

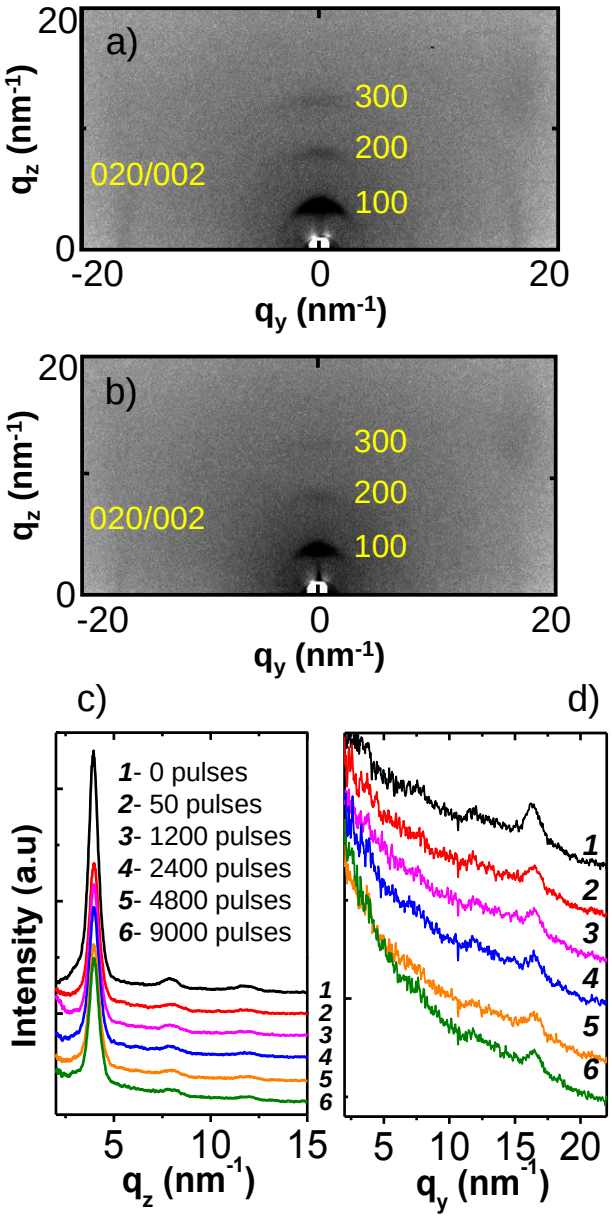

Figure 11. Two dimensional GIWAXS patterns for a) the pristine P3HT thin film and (b) P3HT with LIPSS after irradiation at a fluence of 26 mJ/cm^2 with 4800 pulses. Intensity profiles derived for different number of pulses: c) along the meridian and d) along the equator.

The three meridional reflections *h00* are consecutive orders of the *100* reflection with a *q*-value of 3.8 nm^{-1}. The equatorial weak reflection with a reciprocal scattering vector *q*-value of 16.39 nm^{-1} is attributed to the superposition of the *020* and *002* reflections. In agreement with previous reports [19, 20], crystal structure of P3HT consists of sheets formed by the π–π stacking of the thiophene rings. In addition, the meridional reflections reveal that the P3HT thin film is uniaxially oriented with mainly an edge-on configuration which corresponds to the usual conformation adopted by P3HT thin films consisting of polymer chains parallel to the substrate. A similar orientation is observed for the film with LIPSS. Figure 11 also presents the intensity profiles along the meridian (Figure 11c) and along the equator (Figure 11d), obtained by the radial integration of the 2D GIWAXS patterns as a function of number of pulses. The main result obtained is that the crystalline structure is not significantly affected during LIPSS formation. This effect further supports the indication of chemical stability of P3HT during LIPSS formation, as observed by Raman spectroscopy and NEXAFS and previously discussed. A close inspection of the diffraction patterns reveals that the intensity of both the *100* and the *020/002* peaks, in comparison with those of the pristine sample decreases slightly after 50 pulses and remain essentially constant for the rest of the repetitive irradiation process. As we previously reported, LIPSS formation in polymers proceeds by the heating of the outer polymer surface enhancing polymer dynamics that facilitates the reorganization of the material into the characteristic ripples.[27, 37] Our GIWAXS results suggest that laser irradiation of P3HT induces melting of the polymer surface even at the initial stages of laser irradiation. Moreover, comparison of initial and final GIWAXS patterns indicates a decrease in the crystallinity of LIPSS in relation to the initial thin film as revealed by the reduction of the intensity of the reflections. This explanation is in agreement with the increment of the amorphous phase observed by Raman spectroscopy.

Additionally, by comparison with the C-AFM results (Figure 7), the GIWAXS experiments support the formation of ridges with lower molecular order than that of the original thin film. The ridges are over a continuous P3HT thin film whose initial orientation and crystallinity seems to be unaffected. As a consequence, electrical conduction in the ridges is smaller than in the trenches (Figure 7c). This observation is in agreement with the superficial nature of the LIPSS formation process in which only the outer polymer surface is heated and rearranged, as previously reported. [27]

4. CONCLUSIONS

Laser induced periodic surface structures on poly3-hexylthiophene thin films can be prepared with periods close to the irradiation wavelengths of 532 nm and 266 nm, and by selecting different laser parameters like the fluence and the number of pulses is possible to obtain LIPSS with different depths, periodicities and degree of order. The high optical absorption coefficient of P3HT at 532 nm enables the formation of good quality and well-ordered nanostructures. NEXAFS and Raman spectroscopy measurements reveal a good chemical stability of P3HT thin films under the laser irradiation conditions used for LIPSS formation. Conductive atomic force microscopy shows that in the nanostructures the trenches present a higher conductivity than the ridges. The structural characterization accomplished by *in situ* GIWAXS experiments suggests that, during irradiation melting of the surface takes place leading to a ripple morphology characterized by the existence of low crystallinity and non-conducting ridges over a continuous and more conducting P3HT residual layer whose initial crystallinity seems to be unaffected in comparison to that of the pristine P3HT thin film.

AUTHOR INFORMATION

Corresponding Author

* (A.R.-R.) E-mail alvaro.rodriguez@iem.cfmac.csic.es

* (M.-C.G.-G.) E-mail maricruz@iem.cfmac.csic.es

Notes

The authors declare no competing financial interest.

ACKNOWLEDGEMENTS

The authors gratefully acknowledge the financial support of the Spanish Ministry of Economy and Competitiveness (MINECO) through Projects MAT 2011-23455, MAT 2012-33517 and CTQ 2013-43086-P. A. R-R and E. R. are indebted to MINECO for a FPI (BES-2013-062620) and Ramón y Cajal (RYC-2011-08069) contracts respectively. We thank the Swiss Light Source for beamtime at PolLux, where the NEXAFS experiments were performed. We also thank the ESRF for beamtime at BM26 where *in situ* GISAXS and GIWAXS experiments were carried out. We would like to thank B. Watts for assistance in using beamline PolLux and G. Portale and W.Bras for beamline support at BM26. P. Müller-Buschbaum and S. Guo are thanked for seminal comments at the beginning of this work.

REFERENCES

(1) Bao, Z.; Dodabalapur, A.; Lovinger, A.J. *Appl. Phys. Lett.* **1996,** *69 (26)*, 4108-4110.
(2) Kim, D.H.; Park, Y.D.; Jang, Y.; Yang, H.; Kim, Y.H.; Han, J.I.; Moon, D.G.; Park, S.; Chang, T.; Chang, C.; Joo, M.; Ryu, C.Y.; Cho, K. *Adv. Funct. Mater.* **2005,** *15 (1)*, 77-82.
(3) Zhang, R.; Li, B.; Iovu, M.C.; Jeffries-El, M.; Sauve, G.; Cooper, J.; Jia, S.; Tristram-Nagle, S.; Smilgies, D.M.; Lambeth, D.N.; McCullough, R.D.; Kowalewski, T. *J. Am. Chem. Soc.* **2006,** *128 (11)*, 3480-3481.
(4) Sirringhaus, H.; Brown, P.J.; Friend, R.H.; Nielsen, M.M.; Bechgaard, K.; Langeveld-Voss, B.M.W.; Spiering, A.J.H.; Janssen, R.A.J.; Meijer, E.W.; Herwig, P.; de Leeuw, D.M. *Nature* **1999,** *401 (6754)*, 685-688.

(5) Li, G.; Shrotriya, V.; Huang, J.; Yao, Y.; Moriarty, T.; Emery, K.; Yang, Y. *Nat. Mater.* **2005,** *4 (11)*, 864-868.
(6) Collins, B.A.; Tumbleston, J.R.; Ade, H. *J. Phys. Chem. Lett.* **2011,** *2 (24)*, 3135-3145.
(7) Campoy-Quiles, M.; Ferenczi, T.; Agostinelli, T.; Etchegoin, P.G.; Kim, Y.; Anthopoulos, T.D.; Stavrinou, P.N.; Bradley, D.D.C.; Nelson, J. *Nat. Mater.* **2008,** *7 (2)*, 158-164.
(8) Na, S.-I.; Kim, S.-S.; Jo, J.; Oh, S.-H.; Kim, J.; Kim, D.-Y. *Adv. Funct. Mater.* **2008,** *18 (24)*, 3956-3963.
(9) Yang, Y.; Mielczarek, K.; Aryal, M.; Zakhidov, A.; Hu, W. *Nanoscale* **2014,** *6 (13)*, 7576-7584.
(10) Chen, D.; Zhao, W.; Russell, T.P. *ACS Nano* **2012,** *6 (2)*, 1479-1485.
(11) Vohra, V.; Campoy-Quiles, M.; Garriga, M.; Murata, H. *J. Mater. Chem.* **2012,** *22 (37)*, 20017-20025.
(12) Aryal, M.; Trivedi, K.; Hu, W.W. *ACS Nano* **2009,** *3 (10)*, 3085-3090.
(13) Yang, Y.; Mielczarek, K.; Aryal, M.; Zakhidov, A.; Hu, W. *ACS Nano* **2012,** *6 (4)*, 2877-2892.
(14) Wood, S.; Kim, J.S.; James, D.T.; Tsoi, W.C.; Murphy, C.E.; Kim, J.-S. *J. Chem. Phys* **2013,** *139 (6)*, 064901.
(15) Singh, C.R.; Gupta, G.; Lohwasser, R.; Engmann, S.; Balko, J.; Thelakkat, M.; Thurn-Albrecht, T.; Hoppe, H. *J. Polym. Sci. Part B Polym. Phys.* **2013,** *51 (12)*, 943-951.
(16) Shen, X.; Duzhko, V.V.; Russell, T.P. *Adv. Energy Mater.* **2013,** *3 (2)*, 263-270.
(17) Xin, H.; Reid, O.G.; Ren, G.; Kim, F.S.; Ginger, D.S.; Jenekhe, S.A. *ACS Nano* **2010,** *4 (4)*, 1861-1872.
(18) Jiang, X.M.; Österbacka, R.; Korovyanko, O.; An, C.P.; Horovitz, B.; Janssen, R.A.J.; Vardeny, Z.V. *Adv. Funct. Mater.* **2002,** *12 (9)*, 587-597.
(19) Wu, Z.; Petzold, A.; Henze, T.; Thurn-Albrecht, T.; Lohwasser, R.H.; Sommer, M.; Thelakkat, M. *Macromolecules* **2010,** *43 (10)*, 4646-4653.
(20) Kohn, P.; Rong, Z.; Scherer, K.H.; Sepe, A.; Sommer, M.; Müller-Buschbaum, P.; Friend, R.H.; Steiner, U.; Hüttner, S. *Macromolecules* **2013,** *46 (10)*, 4002-4013.
(21) Hugger, S.; Thomann, R.; Heinzel, T.; Thurn-Albrecht, T. *Colloid Polym. Sci.* **2004,** *282 (8)*, 932-938.
(22) Treat, N.D.; Shuttle, C.G.; Toney, M.F.; Hawker, C.J.; Chabinyc, M.L. *J. Mater. Chem.* **2011,** *21 (39)*, 15224-15231.
(23) Martin, J.; Campoy-Quiles, M.; Nogales, A.; Garriga, M.; Alonso, M.I.; Goni, A.R.; Martin-Gonzalez, M. *Soft Matter* **2014,** *10 (18)*, 3335-3346.
(24) Hlaing, H.; Lu, X.; Hofmann, T.; Yager, K.G.; Black, C.T.; Ocko, B.M. *ACS Nano* **2011,** *5 (9)*, 7532-7538.
(25) Johnston, D.E.; Yager, K.G.; Hlaing, H.; Lu, X.; Ocko, B.M.; Black, C.T. *ACS Nano* **2013,** *8 (1)*, 243-249.
(26) Kim, J.S.; Park, Y.; Lee, D.Y.; Lee, J.H.; Park, J.H.; Kim, J.K.; Cho, K. *Adv. Funct. Mater.* **2010,** *20 (4)*, 540-545.
(27) Rebollar, E.; Perez, S.; Hernandez, J.J.; Martin-Fabiani, I.; Rueda, D.R.; Ezquerra, T.A.; Castillejo, M. *Langmuir* **2011,** *27 (9)*, 5596-5606.
(28) Martin-Fabiani, I.; Rebollar, E.; Perez, S.; Rueda, D.R.; Garcia-Gutierrez, M.C.; Szymczyk, A.; Roslaniec, Z.; Castillejo, M.; Ezquerra, T.A. *Langmuir* **2012,** *28 (20)*, 7938-7945.
(29) Ivanov, M.; Rochon, P. *Appl. Phys. Lett.* **2004,** *84 (22)*, 4511-4513.
(30) Rebollar, E.; Vázquez de Aldana, J.R.; Pérez-Hernández, J.A.; Ezquerra, T.A.; Moreno, P.; Castillejo, M. *Appl. Phys. Lett.* **2012,** *100 (4)*, 041106.
(31) Rebollar, E.; Vazquez de Aldana, J.R.; Martin-Fabiani, I.; Hernandez, M.; Rueda, D.R.; Ezquerra, T.A.; Domingo, C.; Moreno, P.; Castillejo, M. *Phys. Chem. Chem. Phys.* **2013,** *15 (27)*, 11287-11298.
(32) Rebollar, E.; Perez, S.; Hernandez, M.; Domingo, C.; Martin, M.; Ezquerra, T.A.; Garcia-Ruiz, J.P.; Castillejo, M. *Phys. Chem. Chem. Phys.* **2014,** *16 (33)*, 17551-17559.
(33) Kim, Y.; Cook, S.; Tuladhar, S.M.; Choulis, S.A.; Nelson, J.; Durrant, J.R.; Bradley, D.D.C.; Giles, M.; McCulloch, I.; Ha, C.-S.; Ree, M. *Nat Mater* **2006,** *5 (3)*, 197-203.
(34) Chen, C.-P.; Chan, S.-H.; Chao, T.-C.; Ting, C.; Ko, B.-T. *J. Am. Chem. Soc.* **2008,** *130 (38)*, 12828-12833.
(35) Chen, T.-A.; Wu, X.; Rieke, R.D. *J. Am. Chem. Soc.* **1995,** *117 (1)*, 233-244.

(36) Bras, W.; Dolbnya, I.P.; Detollenaere, D.; Van Tol, R.; Malfois, M.; Greaves, G.N.; Ryan, A.J.; Heeley, E. *J. Appl. Crystallogr.* **2003,** *36 (3-1)*, 791-794.
(37) Rebollar, E.; Rueda, D.R.; Martín-Fabiani, I.; Rodríguez-Rodríguez, Á.; García-Gutiérrez, M.-C.; Portale, G.; Castillejo, M.; Ezquerra, T.A. *Langmuir* **2015,** *31 (13)*, 3973-3981.
(38) Müller-Buschbaum, P. In *Applications of Synchrotron Light to Scattering and Diffraction in Materials and Life Sciences*; Gomez, M.; Nogales, A.; Garcia-Gutierrez, M. C.; Ezquerra, T. A., Eds.; Springer-Verlag, Berlin, 2009, Vol. 776, pp 61-89.
(39) Hammersley, A. *FIT2D Website.* http://www.esrf.eu/computing/scientific/FIT2D
(40) Watts, B.; McNeill, C.R. *Macromol. Rapid Commun.* **2010,** *31 (19)*, 1706-1712.
(41) Hitchcock, A.P. *aXis 2000—analysis of X-ray images and spectra.* http://unicorn.mcmaster.ca/aXis2000.html, (2000).
(42) Rebollar, E.; Frischauf, I.; Olbrich, M.; Peterbauer, T.; Hering, S.; Preiner, J.; Hinterdorfer, P.; Romanin, C.; Heitz, J. *Biomaterials* **2008,** *29 (12)*, 1796-1806.
(43) Rebollar, E.; Gaspard, S.; Oujja, M.; Villavieja, M.M.; Corrales, T.; Bosch, P.; Georgiou, S.; Castillejo, M. *Appl. Phys. A* **2006,** *84 (1-2)*, 171-180.
(44) Izumi, T.; Kobashi, S.; Takimiya, K.; Aso, Y.; Otsubo, T. *J. Am. Chem. Soc.* **2003,** *125 (18)*, 5286-5287.
(45) Campaigne, E.; Diedrich, J.L. *J. Am. Chem. Soc.* **1951,** *73 (11)*, 5240-5243.
(46) Meier, H.; Stalmach, U.; Kolshorn, H. *Acta Mater.* **1997,** *48 (9)*, 379-384.
(47) Kanai, K.; Miyazaki, T.; Suzuki, H.; Inaba, M.; Ouchi, Y.; Seki, K. *Phys. Chem. Chem. Phys.* **2010,** *12 (1)*, 273-282.
(48) Watts, B.; Swaraj, S.; Nordlund, D.; Lüning, J.; Ade, H. *J. Chem. Phys* **2011,** *134 (2)*, 024702.
(49) Tsoi, W.C.; James, D.T.; Kim, J.S.; Nicholson, P.G.; Murphy, C.E.; Bradley, D.D.; Nelson, J.; Kim, J.S. *J. Am. Chem. Soc.* **2011,** *133 (25)*, 9834-9843.
(50) Brown, P.J.; Thomas, D.S.; Köhler, A.; Wilson, J.S.; Kim, J.-S.; Ramsdale, C.M.; Sirringhaus, H.; Friend, R.H. *Phys. Rev. B* **2003,** *67 (6)*, 064203.
(51) Shrotriya, V.; Ouyang, J.; Tseng, R.J.; Li, G.; Yang, Y. *Chem. Phys. Lett.* **2005,** *411 (1–3)*, 138-143.
(52) Manceau, M.; Rivaton, A.; Gardette, J.-L.; Guillerez, S.; Lemaître, N. *Polym. Degrad. Stab.* **2009,** *94 (6)*, 898-907.
(53) Furukawa, Y. *J. Phys. Chem.* **1996,** *100 (39)*, 15644-15653.
(54) Shi, G.; Xu, J.; Fu, M. *J. Phys. Chem. B* **2002,** *106 (2)*, 288-292.
(55) Yu, W.; Zhou, J.; Bragg, A.E. *J. Phys. Chem. Lett.* **2012,** *3 (10)*, 1321-1328.
(56) Clark, J.; Silva, C.; Friend, R.H.; Spano, F.C. *Phys. Rev. Lett.* **2007,** *98 (20)*, 206406.
(57) Gao, Y.; Grey, J.K. *J. Am. Chem. Soc.* **2009,** *131 (28)*, 9654-9662.
(58) Gao, J.; Grey, J.K. *J. Chem. Phys* **2013,** *139 (4)*, 044903.

Insert Table of Contents Graphic Here